



Direct measure of dome seeing with a localized optical turbulence sensor

Olivier Lai, J Kanoa Withington, Romain Laugier, Mark Chun

► To cite this version:

Olivier Lai, J Kanoa Withington, Romain Laugier, Mark Chun. Direct measure of dome seeing with a localized optical turbulence sensor. Monthly Notices of the Royal Astronomical Society, 2019, 10.1093/mnras/stz396 . hal-02303520

HAL Id: hal-02303520

<https://hal.science/hal-02303520>

Submitted on 5 Jul 2022

HAL is a multi-disciplinary open access archive for the deposit and dissemination of scientific research documents, whether they are published or not. The documents may come from teaching and research institutions in France or abroad, or from public or private research centers.

L'archive ouverte pluridisciplinaire **HAL**, est destinée au dépôt et à la diffusion de documents scientifiques de niveau recherche, publiés ou non, émanant des établissements d'enseignement et de recherche français ou étrangers, des laboratoires publics ou privés.

Direct measure of dome seeing with a localized optical turbulence sensor

Olivier Lai¹,^{*} J. Kanoa Withington,² Romain Laugier¹ and Mark Chun³

¹Université Côte d'Azur, Observatoire de la Côte d'Azur, CNRS, Laboratoire Lagrange, Bd de l'Observatoire, CS 34229, F-06304 Nice cedex 4, France

²Canada France Hawaii Telescope, 65-1238 Mamalahoa Hwy., Kamuela, HI 96743, USA

³Institute for Astronomy, University of Hawaii, 640 North A'ohōkū Place, Hilo, HI 96720, USA

Accepted 2019 February 5. Received 2019 January 15; in original form 2018 November 22

ABSTRACT

Dome seeing is a known source of image quality degradation for any telescope, but despite tremendous progress in wavefront control through the development of adaptive optics and environmental control through implementation of dome venting, surprisingly little is known about it quantitatively. Circumstantial evidence of prevalent, non-Kolmogorov dome turbulence inferred from turbulence profiles and PSF morphology observed with the `Imaka wide-field adaptive optics system has motivated the development of a new type of optical turbulence sensor called AIR FLOW: Airborne Interferometric Recombiner - Fluctuations of Light at Optical Wavelengths. It is based on a non-redundant mask imaging interferometer that samples the optical turbulence passing through a measurement cell. The instrument measures the local 2D optical Phase Structure Function which is a useful tool to characterize different types of turbulence (Kolmogorov, diffusive turbulence, etc.). By fitting different models, it is possible to determine parameters such as C_n^2 , r_0 , L_0 , or deviation from fully developed turbulence. The instrument was tested in the Canada France Hawaii Telescope dome and the University of Hawaii 2.2-m telescope (UH88) tube. It is ruggedized and sensitive enough to detect changes in the turbulent conditions with different dome vent configurations, as well as slow but large amplitude variations of the index of refraction in the tube of the UH88-inch telescope tube. It can be used to seek out local sources of turbulence inside and around the dome and can be used routinely in an operational setting without affecting observations to quantitatively characterize the local optical turbulence responsible for dome seeing. We believe the instrument could be used in real-time observatory control systems to configure vents and air handlers in ways that more effectively reduce dome seeing. We also believe it could be a tool for site surveys to evaluate dome seeing and dome seeing mitigation strategies *in situ*.

Key words: atmospheric effects – instrumentation: adaptive optics – site testing – techniques: high angular resolution – telescopes.

1 INTRODUCTION

The effects of atmospheric turbulence on telescope image quality have been known since at least the 18th Century by Newton (1730), which led to the development and proliferation of applied adaptive optics (AO) over the last 60 years (Babcock 1953; Roddier 1999). The goal of most AO systems is to simply correct any wavefront aberration it can. Recently the origin of these perturbations has become a subject of special interest because of the challenges they present when designing systems for wide-field AO and high dynamic range imaging.

In the case of wide-field AO, where the AO system tries to correct the wavefront aberrations common to the entire field and

presumably arising from optical turbulence at (or close to) the pupil of the telescope, it has become crucial to determine where the turbulence is introduced in the telescope's beam and to evaluate the relative contribution of the ground layer turbulence versus what is commonly referred to as the free atmosphere. The origins of these sources of turbulence are different; the free atmosphere is generated by wind shear in the troposphere and is usually well characterized by fully developed turbulence (equipartition of turbulent energy at all spatial scales; Kolmogorov 1941) up to an outer scale, while ground layer turbulence is due to the boundary layer between the surface wind and the ground, which is heavily dependent on features of the local topography or obstacles in the airflow. This can lead to different spatial and temporal characteristics of the turbulence that have very different effects on the AO correction and the delivered image quality.

* E-mail: olai@oca.eu

In the case of high dynamic range imaging and extreme AO, the Low Wind Effect (N'Diaye et al. 2018) seen on the Subaru Telescope with the SCExAO instrument and on the VLT with SPHERE had very detrimental consequences on the image quality in what were considered to be excellent observing conditions (low wind, thus slow turbulence). This baffled astronomers until they realized that it was due to radiatively supercooled telescope spiders, which produce a gravity-driven flow of cold air under the spiders and introduce a slight gradient on the phase of each quadrant of the pupil. This was invisible to the AO system due to the phase discontinuity at the location of the spiders in the pupil. Once understood, this problem could be solved at the source by insulating the spiders.

Telescope dome design has also long evolved based on trends in the understanding of aerodynamics, thermal control, and optical turbulence. For example, in the 1970s some domes were designed to insulate the telescopes as much as possible from the outside air (e.g. the dome of the Observatoire du Pic de Midi de Bigorre or of the CFHT), while others tried to match the inside air temperature to the outside (e.g. the Anglo Australian Telescope; Gillingham 1983). In 1991 René Racine confirmed that even a small difference in temperature between the CFH Telescope primary mirror and the surrounding air could significantly degrade the delivered image quality (Racine et al. 1991), and the CFHT dome was thus retrofitted with first a floor cooling system, and eventually with dome vents (Baril et al. 2012; Bauman et al. 2014). The idea of equalizing inside and outside temperatures has once again become very popular, as exemplified by the Gemini telescopes that have large wind vanes in their domes.

Dome design is also subject to conjectural trends; the VLT and Subaru Telescopes have chosen a cylindrical design over the traditional hemispherical design based on wind tunnel testing and hydrodynamical simulations, while the Magellan Telescope's domes have sharp edges with the explicit goal of reducing wake turbulence. The AEOS on Maui and Starfire facility in New Mexico decided to do with their domes completely but are sensitive to wind shake (which telescopes with vents and vanes are also sensitive to in smaller measure). In practice, it is still unclear which design provides the best results. This is slightly vexing but especially critical in the era of extremely large telescopes.

Hydrodynamical simulations have provided some insights into this issue (e.g. Vogiatzis 2011), but the problem is very complex: the telescope environment and the dome geometry, especially the relationship of the dome azimuth to wind direction and speed, are all parameters that can affect the strength and location of turbulence. These simulations also provide insight to where the mechanical turbulence is but this does not necessarily reflect where the optical turbulence may be. The latter can be due to local thermal effects, such as radiative cooling of any part of the telescope or dome, or heat (or cold) sources within or outside the dome.

A better understanding of the impact of the dome and telescope turbulence would allow us to improve the natural image quality of telescopes in a passive way by removing it at the source and would also enhance the performance of AO by reducing the input disturbance, especially where it has a high spatial frequency content which is much harder to correct. Although microthermal probes have been used to detect turbulence, the measurements are less direct and the sensors are delicate. As it is becoming more and more apparent that much of the turbulence seen by the telescopes is indeed self-generated by the structures enclosing them, we think that an empirical approach using a portable, robust optical turbulence sensor has a high potential for reward in improving the soundness of design choices for the future telescope domes.

2 MOTIVATION: EVIDENCE OF SELF-GENERATED AND LOCAL TURBULENCE

2.1 Observations with the `īmaka wide-field adaptive optics instrument

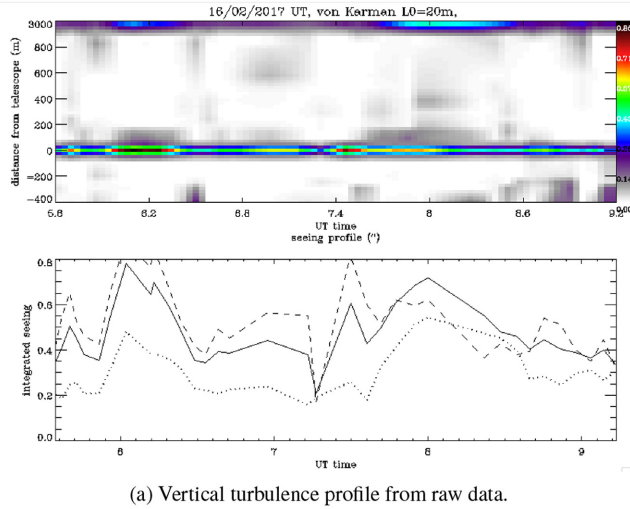
In this section we show that dome turbulence is very detrimental to image quality, especially for very wide-field AO. Although routine and regular measurements of the vertical turbulence profile (e.g. Ziad et al. 2018) can help predict or optimize Ground Layer AO (GLAO) performance, we show that turbulence close to the ground is very different from standard models (i.e. Kolmogorov with a large outer scale compared to the aperture of the telescope, at least >10 m) and needs to be better understood to improve models and performance error budgets of AO systems.

We have developed the `īmaka¹ demonstrator to explore GLAO performance in a variety of conditions (Lai et al. 2008; Chun et al. 2018). The technique of GLAO uses many (>3) guide stars to be able to disentangle the turbulence common to the entire field, which can be corrected by a single corrective element in the pupil, from the uncorrelated turbulence at altitude. Such a configuration makes it possible to retrieve the vertical profile of the turbulence by SloDAR-like methods, i.e. from the statistical correlation of slope wavefront sensor measurements with the altitude dependence provided by triangulation, developed by Wilson (2002). `īmaka is installed on the UH88-inch telescope on Maunakea and saw first light in 2016 October. It can use up to five guide stars on a $0.3^\circ \times 0.4^\circ$ patrol field to feed a 11 arcmin scientific field of view. Performance of the AO can be found in Abdurrahman et al. (2018). An important result of our observations has been to show the importance of dome seeing and self-generated turbulence.

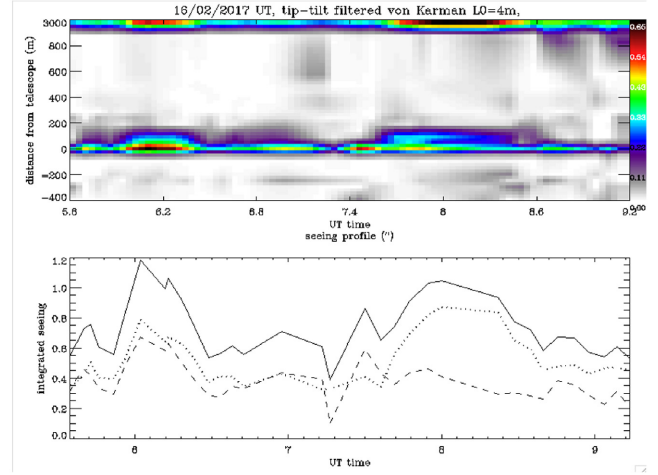
2.2 Reverberation of tube turbulence

Vertical turbulence profiles are obtained by triangulation between different subapertures of wavefront sensors pointed in different directions towards different guide stars. Usually turbulence profiles are computed for positive altitudes above the telescope. However, nothing prevents us from computing the turbulence profile at negative altitudes; this will then scan turbulence below (or after) the pupil such as in the telescope tube. As the instrument is at the Cassegrain focus of the telescope, the beam will cross any layer of turbulence present in the tube three times: A first time as it travels down to the primary mirror, at a small but positive (or zero if the turbulence is exactly at the primary mirror) conjugation altitude; a second time on its way up to the secondary mirror, at a small negative conjugation altitude, and a third time on its way from the secondary mirror to the Cassegrain focus, at a larger negative conjugation altitude. On this last pass, the beam is smaller, so the strength of the turbulence (characterized by D/r_0) should also be smaller. Therefore, there exists a theoretical signature of tube seeing at negative conjugation. In the case of the UH88-inch telescope, when the beam crosses the hole in the primary, it is conjugated to -400 m, and a layer 25 cm above the hole would be seen at -300 m. Due to the geometry of the constellations used with `īmaka, the minimum vertical resolution on the profiles is of the order of 60 m, so we

¹`īmaka means belvedere or scenic viewpoint in the Hawaiian language and refers to the unequaled view of the sky from Maunakea, especially with respect to its superb atmosphere which is particularly favourable for ground layer AO



(a) Vertical turbulence profile from raw data.



(b) Vertical turbulence profile from tip-tilt filtered data which improves the sensitivity of the profile algorithm at the cost of outer scale sensitivity

Figure 1. Turbulence profile for the night of 2017 February 16 (UT). On the lower panels, the integrated seeing is shown as a full line, the ground layer as the dashed line, and the free atmosphere as the dotted line. The tip-tilt filtered profile shows persistent stratification at negative conjugation but in both cases the altitude is compatible with turbulence at the primary mirror, seen after reflection on the secondary as the beam traverses the hole in the primary mirror.

cannot resolve turbulence outside the dome from turbulence inside the tube, or even at small negative conjugations after reflection on the primary mirror. Nonetheless we should easily be able to detect the echo after reflection on the secondary mirror if it is present.

To illustrate this effect, we present turbulence profiles based on observations of the Pleiades obtained on the night of 2017 February 16 using our vertical profile algorithm, described in Lai et al. (2018) in Fig. 1. They reveal transient events at the pupil that have echoes at large negative conjugations. Such events are not rare, but they remain anecdotal. Nonetheless, they indicate that there is most likely turbulence within the tube, which could be explained by the unstable stratification of temperature in the tube, with air heated up by instruments in the Cassegrain environment below colder air entering through the slit and the top of the tube.

2.3 PSF morphology

Analysis of open and closed loop point spread functions (PSFs) also shows the presence of turbulence that is not compatible with fully developed, free atmosphere turbulence, namely Kolmogorov or von Karman with an outer scale at least >10 m. We use a Moffat profile to parametrize the PSFs, with a following form:

$$I(r; \alpha, \beta) = 2 \frac{\beta - 1}{\alpha^2} \left[1 + \left(\frac{r}{\alpha} \right)^2 \right]^{-\beta}. \quad (1)$$

The α parameter is related to the FWHM $= 2\alpha\sqrt{2^{1/\beta} - 1}$ and the β exponent characterizes the wings versus core of the PSF. For example, $\beta = 1$ is a Lorentzian profile, while a Gaussian is approximated as $\beta \rightarrow \infty$. For Kolmogorov turbulence, we can generate an artificial PSF using the simple model:

$$\text{PSF} = \text{FFT} \left[\text{OTF} e^{-\frac{1}{2} D_\phi} \right]; \quad D_\phi = 6.88 \left(\frac{\rho}{r_0} \right)^{\frac{5}{3}}, \quad (2)$$

where ‘OTF’ is the optical transfer function, i.e. the autocorrelation of the pupil function, and D_ϕ is the phase structure function, $D_\phi(\rho) = \langle |\phi(r) - \phi(r + \rho)|^2 \rangle$. From this we can obtain values of full width at half-maximum (FWHM) and β , which are in general agreement with values of β observed at the telescope in turbulence conditions

found in the literature, such as $\beta = 4.765$ (Trujillo et al. 2001). Furthermore, we can also estimate the (FWHM, β) dependence as a function of wavelength and seeing (as shown on Fig. 2).

Fig. 6 of Abdurrahman et al. (2018) shows that open loop images obtained with ‘Imaka’ often have a value of β smaller than 4 (down to 2.5), while higher values are most likely due to vibrations, the effect of which is to sharply increase the value of β , since a Gaussian is approximated as $\beta \rightarrow \infty$. Closed loop images have values systematically smaller than 3.5.

Conversely, we can use an empirical analytical expression from Kellerer (2016) for the von Karman structure function and use a fitting algorithm to extract the atmospheric parameters r_0 and L_0 that best reproduce the observed PSFs.

$$D_{\text{phi}}(r; r_0, L_0) \approx k \left(\frac{L_0}{r_0} \right)^{\frac{5}{3}} \left[1200 + 60 \left(\frac{L_0}{r} \right)^{2.3} + \frac{L_0^{3.4}}{r} \right]^{-\frac{5}{10.2}}. \quad (3)$$

All the stacked PSFs from our 2017 May run were fitted by such parametrized PSFs and we show the results in Fig. 3. We find values of r_0 that are consistent with what might be expected for Maunakea ($0.1 \text{ m} < r_0 < 0.2 \text{ m}$). In open loop, values of the outer scale L_0 vary between 10 and 100 m. However, closed loop values of L_0 are of the order of a few metres. This means that a more significant fraction of the energy is contained in the wings of the PSFs compared to open loop. This is equivalent to a small value of β in the Moffat profiles, as shown on Fig. 2, right.

Such strong wings suggest that the high-frequency content of the spatial power spectral density is substantial. It is of great interest to GLAO performance assessment whether the strong wings (and the effective reduction of the outer scale as a parametrization of ground layer correction) are intrinsic to GLAO performance, or whether they are due to the tube and dome seeing of the UH88"-inch telescope on which these observations were carried out. For all these reasons, we decided to build a portable optical turbulence sensor that could be placed within the telescope tube, or inside the dome to obtain an unambiguous and quantitative measure of the optical turbulence seen by the telescope.

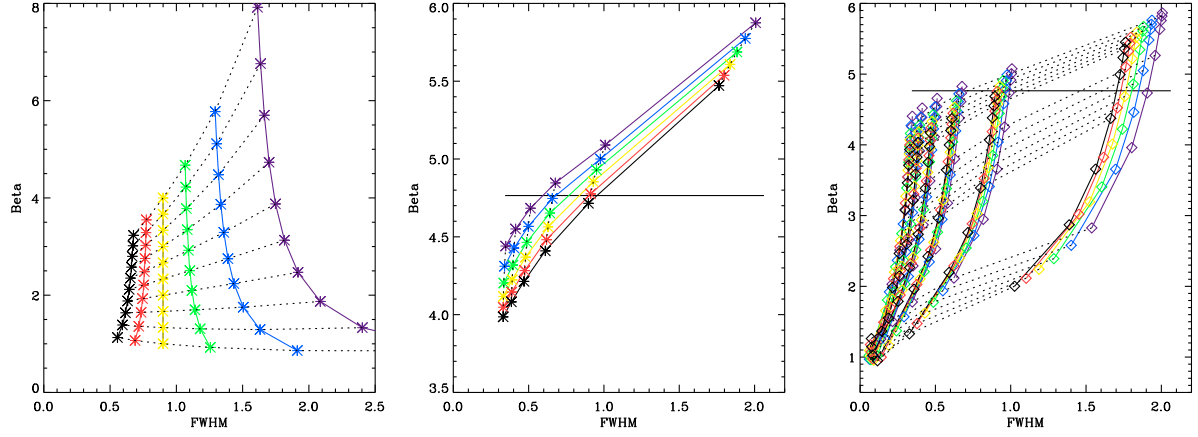
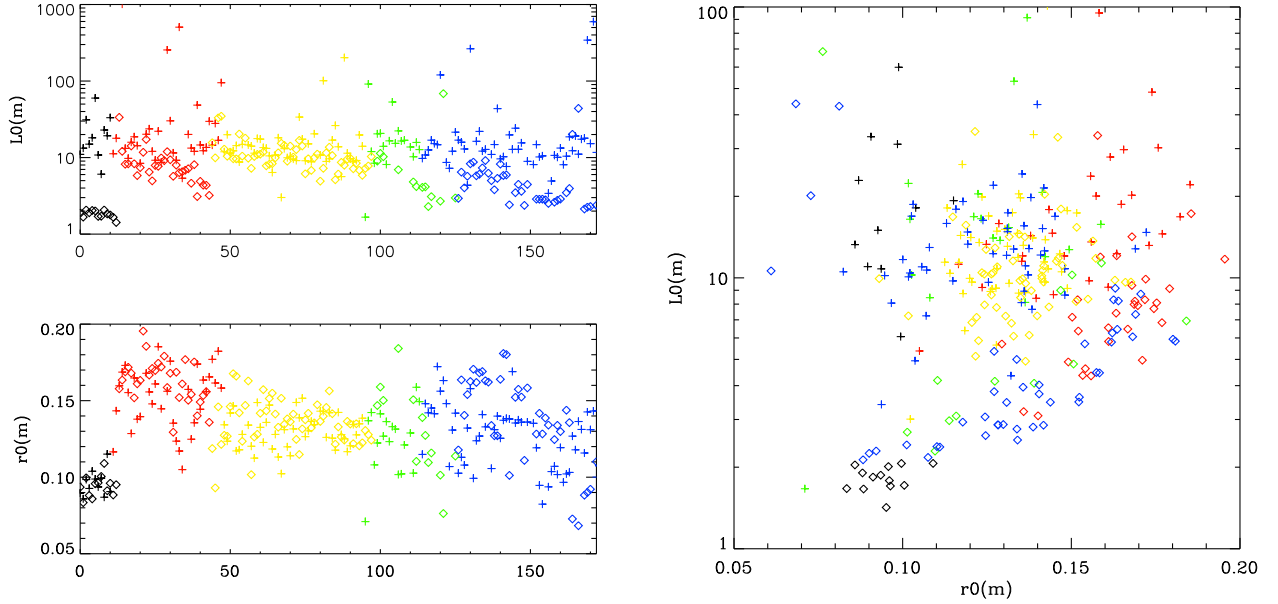


Figure 2. left-hand panel, dependence of Moffat profile with wavelength. A Moffat PSF with $\text{FWHM} = 0.9$ arcmin is generated at 800 nm (yellow vertical line) for 10 values of β between 1 and 4. The locus of coloured lines shows how FWHM and β vary for 500 nm (purple), 600 nm (blue), 700 nm (green), 900 nm (red), and $1 \mu\text{m}$ (black) when the phase structure function is proportional to λ^{-2} . Centre, the (FWHM, β) locus for Kolmogorov turbulence for the same wavelengths (same colour coding) with $r_0 = 30, 25, 20, 15, 10$, and 5 cm from left to right. The black dashed line shows the value of 4.765 from Trujillo et al. (2001). Right-hand panel, including the outer scale (with $L_0 = 2, 5, 10, 20, 50, 100, 200$, and 1000 m) with the same values of r_0 as the previous panel dramatically decreases the value of β as L_0 decreases.



(a) Sequential display of L_0 (top) and r_0 (bottom).

(b) L_0 (logarithmic) versus r_0 (linear) for all nights.

Figure 3. von Karman parametric fit to stacked PSFs for the 2017 May run: 17th in black, 18th in red, 19th in yellow, 20th in green, and 21st in blue. Crosses are open loop and diamonds are closed loop. Values of L_0 are systematically smaller in closed loop and r_0 is generally somewhat larger.

3 METHOD

The simplest concept to measure optical turbulence is to measure the optical path difference (OPD) between two parallel beams. If the beams are made to interfere, the OPD introduced by the turbulence can be measured with the phase shift of the interferogram. In fact, nothing limits the technique to two beams as long as the different interference patterns (due to different baselines between pairs of beams) in the focal plane can be disentangled and their phase extracted. We therefore borrowed non-redundant masks from the theory of aperture masking (e.g. Kulkarni 1988), as they allow us to recover individual spatial frequencies unambiguously from a simple Fourier transform. Different separations of the holes in the

non-redundant mask provide the phase for different baselines and measuring the variance of this phase as a function of the separation of the beams provides the phase structure function D_ϕ . Models of the phase structure functions (Kolmogorov, equation 2; von Karman, equation 3; variable exponent, etc.) allow us to parametrize the measurements of optical turbulence: we cannot only measure the structure constant C_n^2 , but also test whether the turbulence is fully developed and even whether the fluctuations of the index of refraction are turbulent (pure tip-tilt is generated when there is no mixing of different temperature air-masses and the associated phase structure function is proportional to r^2). The data processing will therefore try to fit different models to the measured phase structure

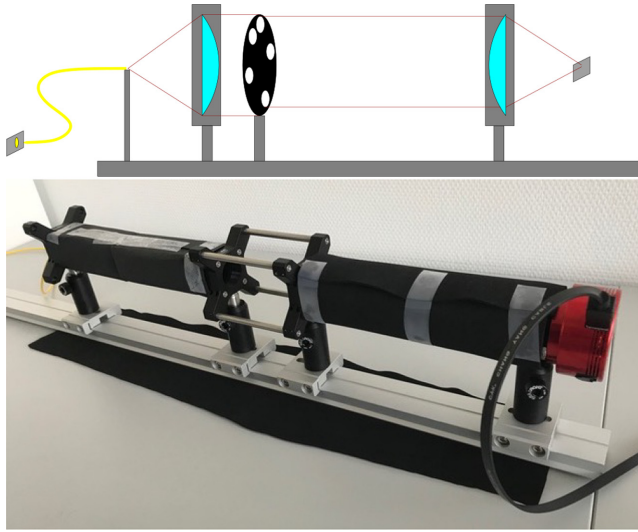


Figure 4. AIRFLOW concept (top) and instrument (bottom). A source is reimaged on to a detector with a non-redundant mask placed in the collimated turbulence sampling cell. The device has to be structurally rigid, which is achieved with an I-beam geometry.

function along its major and minor axis (the phase structure function is measured in two dimensions perpendicular to the propagation axis). The implementation of a very rigid mechanical structure has so far limited the beam separation to 25 mm (see Section 3.1), which makes the measurement relatively insensitive to outer scale effects. Although there is much information in the deviations from the Kolmogorov phase structure function, we have thus far limited the analysis to Kolmogorov turbulence to provide homogeneous measurements and to be able to compute the structure constant C_n^2 , which is defined in the context of this model. To obtain the C_n^2 from r_0 we define the baseline b as the separation between the beams and the propagation distance L is the distance over which the turbulence is sampled; the propagation distance has to be sufficiently large to prevent self-induced turbulence but small enough to measure local refractive index structure constant, C_n^2 . We note in passing that r_0 does not have a physical significance other than the diameter of a region where the phase variance is equal to 1 radian²; the baseline can therefore be much smaller than r_0 without affecting the accuracy of the measurement, since what we are really measuring is C_n^2 . In fact, r_0 is an integrated measure of C_n^2 along the propagation distance:

$$r_0 = \left[0.423k^2 \int_0^L C_n^2(h) dh \right]^{-\frac{3}{5}}, \quad (4)$$

where k is the wavenumber. For a plane wave and constant C_n^2 , the Fried parameter simplifies to

$$r_0 = 1.68 (k^2 C_n^2 L)^{-\frac{3}{5}}. \quad (5)$$

With L and k known and r_0 obtained from the fit to the measured phase structure function, we can thus compute C_n^2 .

3.1 AIRFLOW instrument

The sensor was developed using off-the-shelf components and is shown in Fig. 4. A laser diode is coupled to a single mode fibre to produce a point source on one side of an optical cage. The beam is collimated by a plano-convex lens, and a 3D printed non-redundant

mask with nine holes is inserted in the beam. A second plano-convex lens reimages the fringe pattern with a 1:1 magnification on to a commercial (ZWO AS178MM) CMOS camera with small (2.4 μ m) pixels, low read noise ($< 2e^-$ /pixel), 14 bit ADC, and high-frame rate (200 Hz with a 256×256 raster). Currently, the sampling cell measures 100 mm and the entire sensor fits on a 500 mm bench.

Future versions may include a two lens solution to shorten the arms before and after collimation, enabling a larger (both in length and diameter) turbulence sampling cell within the same envelope. We are also considering a design with the fibre and camera on the same side, and a corner cube at some arbitrary location to return the beam, although it is possible that having the reflector mechanically dissociated from the rest of the instrument may lead to increased sensitivity to vibrations.

3.2 Data processing

Sequences of thousands of images are acquired at rates as high as 200 Hz. Eventually the frame rate will be optimized for the experiment. Dome turbulence monitoring requires only a low-frame rate but pointed experiments such as the study of the characteristics of tube seeing or of developing turbulence, will benefit from a higher frame rate. We have chosen a nine-hole (Fig. 5) design that generates 36 baselines but have also experimented with 7 and 18 holes. The mask we used is a standard Golay 9 pattern (Golay 1971) and produces non-redundant baseline vectors in 2D which evenly fills the frequency plane, even if the modulus of many of these baselines is the same. We compute the complex Fourier transform of each image and each spatial frequency is identified and the phase is recorded into a cube. The variance of the phase is then computed and when plotted against the baseline vector, it directly provides the 2D phase structure function of the optical index of refraction; the azimuthal asymmetry provides information on the anisotropy of the turbulence.

For ease of use in the field, we have developed a GUI-based data reduction software that reduces the camera data into phase files, which can then be filtered (events or temporal frequencies associated with vibrations) and analysed using different models (shown in Fig. 6).

4 RESULTS

After laboratory testing and optimization, we tested the instrument during a two period in 2018 October on Maunakea in the Canada France Hawaii Telescope's dome that has retrofitted its dome with six vents on each side of the dome slit, as well as in the UH telescope tube. These tests were exploratory and not carried out in ideal conditions. For example, measurement locations were limited by physical access and we wanted to mitigate any risk of stray light contamination from the instrument. However, the results we obtained unequivocally demonstrate that this instrument is sufficiently ruggedized and sensitive enough to detect changes in the turbulent conditions with different dome vent configurations and could, by properly characterizing the site, be used to routinely improve the telescope's environment.

4.1 CFHT

The CFHT dome is of particular interest due to the recent retrofit of dome vents on both sides of the slit. These vents can be actuated individually and have (vertical) deflectors built-in in their vanes. What they lack however is a quantitative way to measure the effect

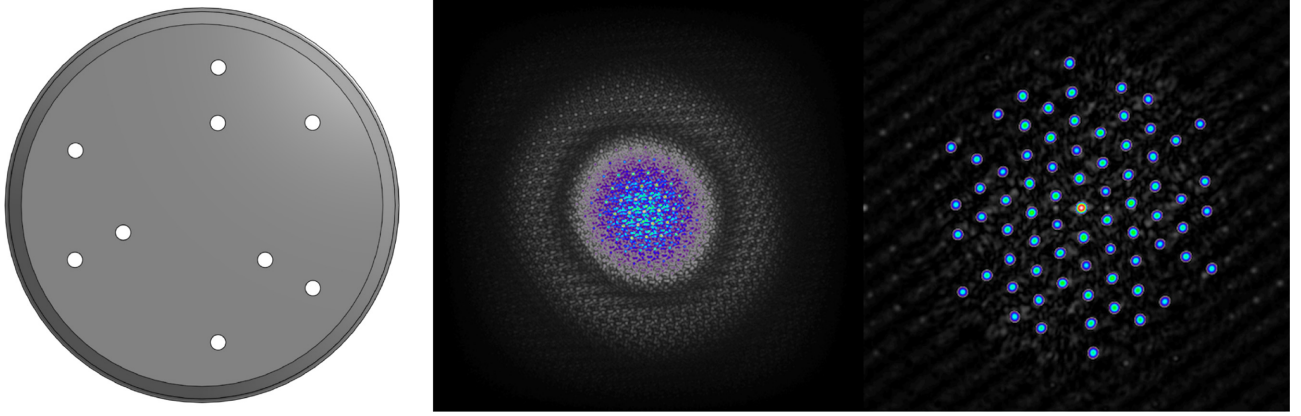


Figure 5. The nine-hole non-redundant mask (left-hand side) produces the convolution of 36 fringe patterns in the PSF (centre), the PSF of which the Fourier Transform (of which the modulus squared, i.e the autocorrelation of the mask is shown on the right-hand side) produces clearly identifiable spatial frequencies for which the phase can be recorded.

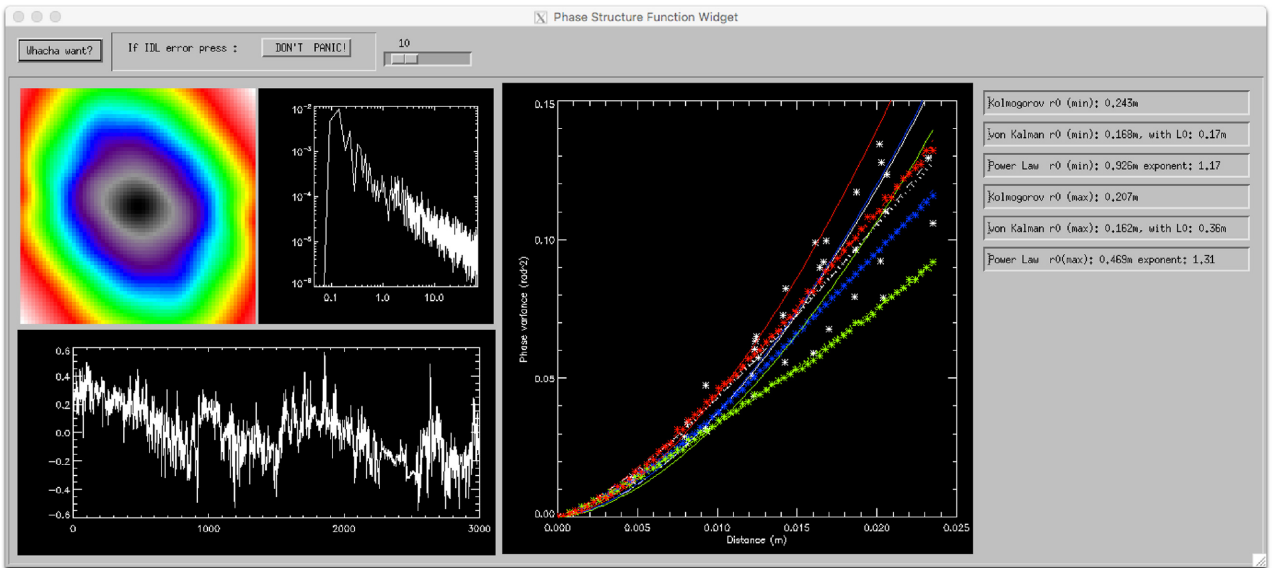


Figure 6. GUI-based data processing software that generates the 2D phase structure function as well as various model fits to the data.

of opening or closing vents in different configurations. It is clear that opening the vents at the start of the night helps to thermalize the dome much faster and reduces slit seeing caused by warm inside air rising and mixing with cold outside air just in front of the telescope beam (Bauman et al. 2014). The common rule used to operate the vents is to open them as much as possible until image quality degrades from windshake. Our goal with these tests was to determine whether we could detect changes in the turbulence level when the environment of the dome was altered with dome vents.

4.1.1 Daytime tests

We installed the AIRFLOW instrument on the CFH Telescope South-East truss on Thursday 2018 October 4, for daytime testing. The telescope truss was chosen due to its proximity to the telescope's beam and because it could potentially measure turbulence carried by air entering the dome from the vents. The conditions were certainly unfavourable (in the sense of strong turbulence, but favourable for

our tests of AIRFLOW's ability to detect changes in turbulence when operating the vents), as it was sunny outside with the ground being energetically heated, and there were 20 knots wind from the North East. Once the sensor was in position, we obtained the first data set with the dome slit and vents closed as a baseline, as the dome was quiet and undisturbed. The sequence of observation was to open the dome slit (to about 2/3), then to open the East vents, followed by the West vents, and finally to close the East vents while leaving the West vents open. The results are shown in Fig. 7.

With the dome closed, the dome environment felt very quiet and values of C_n^2 were of the order of $10^{-15} m^{-2/3}$. When the slit was opened, a few measurements showed stronger turbulence above the baseline level, suggesting that a few turbulent vortices had come into the dome. This was consistent with our anecdotal observations: one could indeed feel intermittent buffeting while standing on the scissor lift next to the Caisson Central. When the East vents were opened, the turbulence level rose dramatically to levels of $C_n^2 \sim 10^{-13} m^{-2/3}$, but this may not be so surprising, as these were upwind and daytime turbulence over the heated ground may have come into the dome carried by the steady wind. This behaviour was even

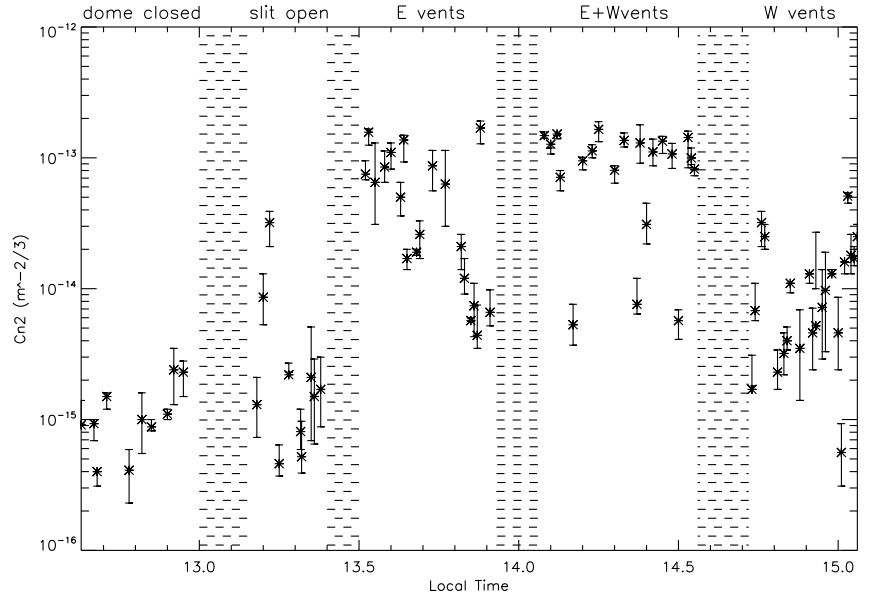


Figure 7. Left-hand side: The sensor on the South-East telescope truss above the Caisson Central. Right-hand side, measurements of the C_n^2 during daytime dome vent operations. Note that the error bars refer to the minimum and maximum axes of the phase structure function; small error bars thus refer to isotropic turbulence.

more pronounced when the West vents were opened. Although our data set is limited, there appears to be a bimodal aspect to the data between 13.5h and 14.5h: One branch seems to decay when the East vents were opened, as if the dome were thermalizing and reverting to laminar flow, while another branch remains high, as one would expect if turbulent cells carried by the wind were crossing the beam intermittently. This latter behaviour was more pronounced when the West vents were opened, which tends to support this hypothesis. Finally, when the East (upwind) vents were closed and the West (downwind) vents remained open, this behaviour stopped, and the turbulence level decreased, although with still relatively large fluctuations.

4.1.2 Endurance test

We also installed AIRFLOW on a pole on the mezzanine by the telescope South pier on Tuesday, October 9 until the morning of Thursday 11. The location was not ideal because the sensor was below the level of the Caisson Central and quite far away from the telescope beam (Fig. 8, left-hand panel). Furthermore, the dome vents were not in use during those two nights and the sensor was relatively close (3~4 m) from the dome wall, so it is most likely not representative of the turbulence seen by the telescope. However, the goal of these tests was to confirm autonomous and continuous operation of the sensor and we therefore wanted easier access than the telescope truss. On the night of the 9th, the seeing reported by the autonomous Mauna Kea Atmospheric Monitor (MKAM²) DIMM seeing monitor was reasonable (between 0.4 and 0.6 arcsec), while the image quality (IQ) reported by the instrument at the CFHT Cassegrain focus that night (SITELLE) was of the order of 1~1.4 arcsec in the second half of the night (and much worse in the first half). This discrepancy would most likely have been due to dome seeing, especially as there was almost no wind and the

dome vents were not operational. During the first half of the night, we were trying to automate the operation and reduction of the sensor, so our automatic data capture started just after midnight and operated continuously until we unmounted it on Thursday morning.

The results of the automatic data processing for the entire 33 hr are shown in Fig. 8 (right-hand panel). We also show the comparison between the MKAM DIMM, the SITELLE IQ, and the AIRFLOW measurements for the second half of the night of the 9th in Fig. 9. One would have expected the difference in SITELLE IQ and DIMM to be due to dome seeing, but unfortunately the AIRFLOW sensor was probably too far from the telescope beam, and too close to the dome wall to be truly representative. Note, however, that when the image quality blew up in the very last hour of the night, the AIRFLOW measurements also became erratic.

4.2 UH88-inch tube

On Thursday October 11, we carried out tests inside the UH88-inch telescope tube as we suspect that there is temperature stratification within the tube, which is possibly leading to turbulence due to the instability of cold air coming in at the top of the tube and warmer air at the bottom. The telescope was tilted over towards the South to an elevation of about 30° so that we could access the tube from the South pier (see Fig. 10, left-hand panel). We first lowered the sensor into the tube from the top, but we had to go inside the tube to be able to bring it all the way down to the primary mirror. Measurements from this series are not included because the presence of a warm body inside the tube had disturbed the air and produced relatively high levels of turbulence. We let the air settle for about 45 min before measuring the turbulence along the tube by pulling the sensor up with a rope in two series of measurements, which were repeatable. These results are shown in Fig. 10, middle. Finally, we opened the slit and took measurements with the sensor at the edge of the tube and at the slit, which can also be seen in the top middle panel

²<http://mkwc.ifa.hawaii.edu/current/seeing/>



Figure 8. Left-hand panel, the sensor on a pole on the mezzanine by the South pier; the location is not ideal because it is below the Caisson Central and close to the dome wall. Right-hand panel, C_n^2 measured during 33 consecutive hours; daytime (slit closed) is shown as hatched.

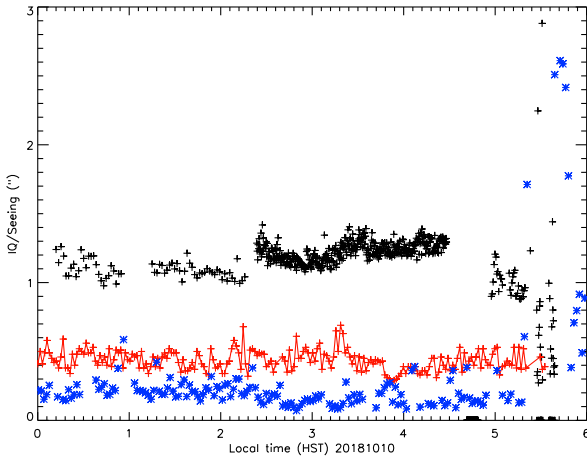


Figure 9. Comparison of the IQ delivered at the telescope (black crosses), the DIMM measurement of integrated atmospheric seeing (red line), and our sensor measurements (blue stars) translated to seeing within an arbitrary constant. The lack of agreement is most likely due to the location of the sensor, but such tests are invaluable to confirm that the sensor provides a representative measurement of seeing.

of Fig. 10, at a level of a few $10^{-12} \text{m}^{-2/3}$. This high level is not surprising given the large temperature difference between inside the dome and the outside air, actively heated by the sun.

The quantitative values obtained from our measurements are consistent with the imaka image quality analysis, from which we infer that the dome seeing is of the order of 0.3–0.4 arcsec. If we assume that all the dome seeing takes place inside the tube, and consider a constant C_n^2 inside the tube at a level of $3 \times 10^{-14} \text{m}^{-2/3}$,

with a 5 m length tube, using equation (5) we find an integrated r_0 of 0.25 m, which corresponds to a value of dome seeing of 0.4 arcsec.

There also appears to be a trend that the C_n^2 seems to be larger close to the primary mirror than at the top of the tube. This could be due to more efficient mixing of warm and cold air close to the top of the tube than at the primary mirror, where pockets of different temperature appear to slosh around randomly. This is corroborated by the very different temporal characteristics of the measured turbulence, shown in the right-hand panel of Fig. 10, where we see that the air is generally calm close to the primary mirror, with large amplitude, slow events coming through, while the turbulence is much faster in the dome slit. Thus, it may be interesting to use a fan (!) or to open the access panels next to the primary mirror during observing to breakup the coherent air movement in the tube, allowing air at different temperatures to mix more efficiently and to homogenize the index of refraction.

5 DISCUSSION

We find the results of these exploratory tests to be very satisfactory in demonstrating the dynamic and sensitivity range of the sensor. The sensor measures changes in C_n^2 consistent with the environment (e.g. quiet during the day, capable of measuring a change when the slit is open). However, there are two further tests that would be very convincing and would improve our confidence that the measurements provided by AIRFLOW are a direct measure of image quality degradation from local seeing, should further demonstration be required. The first is to repeat the comparison of the difference between instrument-delivered IQ minus DIMM seeing to the AIRFLOW measurements. However, this test will only be useful if carried out consistently over a broad range of conditions

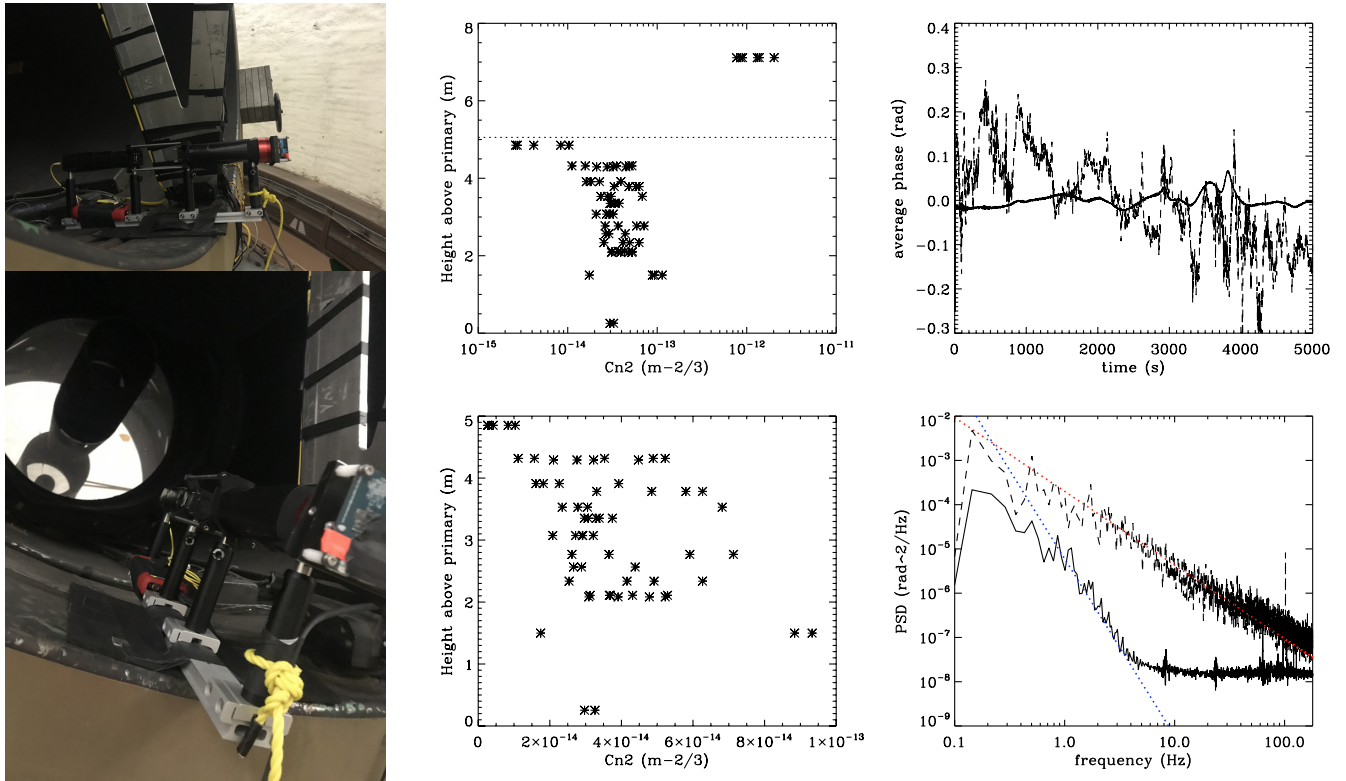


Figure 10. Left-hand panel, AIRFLOW in the UH88 telescope tube. A rope was used to pull the sensor without disturbing the air inside the tube. Middle, C_n^2 versus height above the primary mirror (the dotted line shows the top of the tube) in log scale at the top and linear scale at the bottom. Right-hand panel, the temporal behaviour of the turbulence at the slit (dashed line) and close to the primary mirror (full line), shown as a time series (top) and power spectral density (bottom). The fit (dotted lines) for turbulence at the slit is proportional to $f^{-5/3}$, while it is proportional to f^{-4} close to the primary mirror.

and systematically over longer periods of time on the telescope truss. Such tests are being discussed but require care to not interfere with telescope operations or performance. A second test could be to install an AIRFLOW sensor on the MKAM telescope and compare the difference between DIMM and MASS to its measurements. This would confirm that the ground layer can be measured directly (barring the assumption that MASS provides an accurate measure of the free atmosphere); for such a test, a weather-resistant sensor is being developed.

Also, further tests of simultaneous use of AIRFLOW with the *imaka* instrument are planned, with the goal of confirming whether the negative conjugation echoes of Fig. 1 can be confirmed by direct detection. Ideally, three sensors (one at the primary, one at the top of the tube, and one at the slit, or a single sensor movable on a rail along the telescope tube) would be most useful for such an experiment to get a more comprehensive picture of air mixing and turbulence inside the telescope and the dome.

6 CONCLUSIONS

We have developed a new type of optical turbulence sensor that we have named AIRFLOW and which samples turbulence through the optical path differences along beams arranged in a non-redundant pattern. The variance of the phase variations as a function of separation is a direct measure of the 2D phase structure function, which we can use to fit different turbulence models and to analyse the temporal properties of the signal. We have demonstrated that the sensor was capable of measuring physically meaningful changes of levels of turbulence when the environment was altered (i.e. by

opening dome vents). Motivation to build this sensor arose from strong but indirect evidence of local or self-generated turbulence that we were able to disentangle from the atmospheric turbulence using the *imaka* instrument. Dome and telescope seeing is the only source of disturbance to image quality that we can correct directly at the source, provided we can measure it and measure the effects of whatever means we might use to breakup temperature differences carried by air cells. Every telescope and every dome are different, so solutions may be quite different for each environment. For telescopes with venting solutions, such as Gemini, CFHT, Subaru, or UKIRT, optimal strategies can now be developed by obtaining direct measurements of turbulence crossing the telescope's beam. For other telescopes, solutions might include hedges, deflectors, foils, or fans. Providing directly measured real-time feedback at a low cost opens the way to a better understanding of the genesis and evolution of these disturbances and to the development of both more relevant design choices at the drawing board, and more effective control strategies during observations. It therefore constitutes an important step towards minimizing the problem directly at its source.

ACKNOWLEDGEMENTS

We wish to thank Kevin Ho and the daycrews of the CFHT and UH88 telescopes for support at every step of installation. We also wish to thank the CFHT executives who welcomed us and provided access to the telescope. This research was funded by funding from Observatoire de la Côte d'Azur through its Budget Qualité Recherche (BQR) and Université Nice Sophia-Antipolis through its Crédit Incitatif à la Recherche (CSI) program.

REFERENCES

- Abdurrahman F. N., Lu J. R., Chun M., Service M. W., Lai O., Föhring D., Toomey D., Baranec C., 2018, *AJ*, 156, 100
- Babcock H. W., 1953, *PASP*, 65, 229
- Baril M., Benedict T., Thanjavur K., Salmon D., Vogiatzis K., Racine R., Breidenthal R., 2012, in Angeli G. Z., Dierickx P., eds, Proc. SPIE Conf. Ser. Vol. 8449, Modeling, Systems Engineering, and Project Management for Astronomy V. SPIE, Amsterdam
- Bauman S. E. et al., 2014, in Peck A. B., Benn C. R., Seaman R. L., eds, Proc. SPIE Conf. Ser. Vol. 9149, Observatory Operations: Strategies, Processes, and Systems V. SPIE, Bellingham, p. 914927.
- Chun M. et al., 2018, in Close L. M., Schreiber L., Schmidt D., eds, Proc. SPIE Conf. Ser. Vol. 10703, Adaptive Optical Systems. SPIE, Austin TX, p. 7
- Gilligam P. R., 1983, in Barr L. D., Mack B., eds, Proc. SPIE Conf. Ser. Vol. 444, Advanced Technology Optical Telescope II. SPIE, London, England, p. 10
- Golay M. J., 1971, *J. Opt. Soc. Am.*, 61, 272
- Kellerer A. N., Ribak E. N., 2016, *Opt. Lett.*, 41, 3181
- Kolmogorov A., 1941, *Dokl. Akad. Nauk*, 30, 301
- Kulkarni S., 1988, *ESO Conf. Workshop Proc.*, 29, 595
- Lai O. et al., 2008, in Hubin N., Max C. E., Wizinowich P. L., eds, Proc. SPIE Conf. Ser. Vol. 7015, Adaptive Optics Systems. SPIE, Marseille, p. 12
- Lai O., Chun M., Abdurrahman F., Lu J., Service M., Föhring D., Toomey D., 2018, in Close L. M., Schreiber L., Schmidt D., eds, Proc. SPIE Conf. Ser. Vol. 10703, Adaptive Optical Systems. SPIE, Austin, TX, p. 14
- N'Diaye M., Martinache F., Jovanovic N., Lozi J., Guyon O., Norris B., Ceau A., Mary D., 2018, *A&A*, 610, A18
- Newton A. N., 2013, *Opticks, or, A Treatise of the Reflections, Refractions, Inflections & Colours of Light*, 4th edn. William Innys, London
- Racine R., Salmon D., Cowley D., Sovka J., 1991, *PASP*, 103, 1020
- Roddier F., 1999, *Adaptive Optics in Astronomy*. Cambridge Univ. Press, Cambridge
- Trujillo I., Aguerri J. A. L., Cepa J., Gutiérrez C. M., 2001, *MNRAS*, 328, 977
- Vogiatzis K., 2011, in Andersen T., Enmark A., eds, Proc. SPIE Conf. Ser. Vol. 8336, Aero-thermal Modeling Framework for TMT. SPIE, Bellingham, p. 8336
- Wilson R. W., 2002, *MNRAS*, 337, 103
- Ziad A., Chabé J., Fanteu-Caujolle Y., Aristidi E., Renaud C., Ben Rahhal M., 2018, in Close L. M., Schreiber L., Schmidt D., eds, CATS: An Autonomous Station for Atmospheric Turbulence Characterization. SPIE, Bellingham, p. 10703

This paper has been typeset from a \LaTeX file prepared by the author.